Mon. Not. R. Astron. Soc. **000**, 1–9 (0000) Printed 10 June 2015 (MN LaTeX style file v2.2)

High resolution imaging and spectroscopy of the gravitational lens SDSSJ1206+4332: a natural coronagraph at $z = 1.789$ and a standard ruler at $z = 0.745$

Adriano Agnello[1⋆], Alessandro Sonnenfeld[1], Sherry H. Suyu[2], Tommaso Treu[1,†], Christopher D. Fassnacht[3], Charlotte Mason[4], Maruša Bradač[3], Matthew W. Auger[5]

[1] *Department of Physics and Astronomy, PAB, 430 Portola Plaza, Box 951547, Los Angeles, CA 90095-1547, USA*
[2] *Institute of Astronomy and Astrophysics, Academia Sinica, P.O. Box 23-141, Taipei 10617, Taiwan*
[3] *Department of Physics, University of California Davis, 1 Shields Avenue, Davis, CA 95616, USA*
[4] *Department of Physics, University of California, Santa Barbara, CA 93106, USA*
[5] *Institute of Astronomy, Madingley Road, Cambridge CB3 0HA, UK*
† *Packard Fellow.*

arXiv:1506.02720v1 [astro-ph.CO] 8 Jun 2015

Accepted . Received

ABSTRACT

We present spectroscopy and laser guide star adaptive optics (LGSAO) images of the doubly imaged lensed quasar SDSS J1206+4332. We revise the deflector redshift proposed previously to $z_d = 0.745$, and measure for the first time its velocity dispersion $\sigma = (290 \pm 30)$ km/s. The LGSAO data show the lensed quasar host galaxy stretching over the astroid caustic thus forming an extra pair of merging images, which was previously thought to be an unrelated galaxy in seeing limited data. Owing to the peculiar geometry, the lens acts as a natural coronagraph on the broad-line region of the quasar so that only narrow [O III] emission is found in the fold arc. We use the data to reconstruct the source structure and deflector potential, including nearby perturbers. We reconstruct the point-spread function (PSF) from the quasar images themselves, since no additional point source is present in the field of view. From gravitational lensing and stellar dynamics, we find the slope of the total mass density profile to be $\gamma' = -\log\rho/\log r = 1.93 \pm 0.09$. We discuss the potential of SDSS J1206+4332 for measuring time delay distance (and thus H_0 and other cosmological parameters), or as a standard ruler, in combination with the time delay published by the COSMOGRAIL collaboration. We conclude that this system is very promising for cosmography. However, in order to achieve competitive precision and accuracy, an independent characterization of the PSF is needed. Spatially resolved kinematics of the deflector would reduce the uncertainties further. Both are within the reach of current observational facilities.

Key words: gravitational lensing: strong – quasars: emission lines – galaxies: kinematics and dynamics – cosmology: distance scale – methods: observational – methods: statistical

1 INTRODUCTION

In the past two decades, the dream of Refsdal (1964) to use gravitational time delays as a tool for cosmography has become a reality. Several observational and modeling breakthroughs now make it possible to measure time delay distances with 5-6% precision and accuracy from a single galaxy scale gravitational lens system (e.g. Suyu et al. 2010), and the angular diameter distance to the deflector (Paraficz & Hjorth 2009; Jee et al. 2014). In turn, these absolute distance measurements enable the determination of the Hubble Constant (e.g., Schechter et al. 1997; Treu & Koopmans 2002; Wucknitz et al. 2004; Jackson 2007; Oguri 2007), and other cosmological parameters like flatness and equation of state of dark energy when combined with other probes (Suyu et al. 2013, 2014). The necessary observational ingredients include determination of time delays with few percent precision (Burud et al. 2002; Fassnacht et al. 2002; Eulaers et

⋆ aagnello@astro.ucla.edu, tt@astro.ucla.edu

© 0000 RAS

al. 2013; Tewes et al. 2013), imaging and astrometry at 10-100 mas resolution (Fassnacht et al. 2002; Koopmans et al. 2003; Chantry et al. 2010), stellar velocity dispersion of the deflector (Treu & Koopmans 2002), and imaging and spectroscopy to characterize the line of sight and environment (Keeton & Zabludoff 2004; Fassnacht et al. 2011; Greene et al. 2013; Collett et al. 2013).

The application of lensed quasars for cosmography has been limited by the small number of systems for which the full complement of data is available. We present here results from on ongoing program, aimed at increasing the statistical power of the method, by obtainining all the required imaging and spectroscopic data for gravitational lensed quasars with measured time delays.

In this paper, we focus on a very unusual and remarkable system, the doubly lensed quasar SDSS J1206+4332. It was discovered by Oguri et al. (2005), who suggested a redshift of $z = 0.748$ for the lens galaxy based on Mg II absorption on the quasar spectra, and has been monitored by Eulaers et al. (2013) to obtain a time-delay $\Delta t = 111 \pm 3$ days between the two quasar images. In those observations, an additional galaxy 'G3' was detected along the line of sight NE of the system, which would complicate the lens modelling. Our laser guide star adaptive optics (LGSAO, Wizinowich et al. 2006) data show that 'G3' is in fact two merging images of lensed quasar host galaxy itself. In practice, while the quasar is just outside the astroid caustic and thus only doubly imaged, the host galaxy cross the caustics and produces four images in a fold configuration. This configuration makes this system very interesting for cosmography, since it is relatively easy to monitor as a double, and yet it has a larger number of imaging constraints available for reconstructing the lensing potential than a typical pure double.

We complement our LGSAO data with long-slit spectroscopy of the deflector, whence we can revisit the redshift and provide the first measurement of the velocity dispersion. Spectroscopy and high-resolution imaging enable the reconstruction of source structure and inference of the gravitational lens potential. Together with the published time-delay, they enable us to assess the role of SDSS J1206+4332 as a probe of the Hubble constant, or alternatively as a standard ruler.

This paper is structured as follows. In Section 2 we describe the imaging data, complemented with the spectroscopic follow-up in Section 3. In Section 4, we illustrate the reconstruction of deflector, source and PSF. We add information form stellar kinematics in Section 5, obtaining an independent characterization of the deflector total mass density profile. We then discuss the value of SDSS J1206+4332 for cosmography, in terms of inference on H_0 and deviations from the flat ΛCDM paradigm. We conclude in Section 7.

2 KECK ADAPTIVE-OPTICS IMAGING

We imaged SDSS J1206+4332 in the K′ band at 2.2μm with the NIRC2 camera on Keck II on 2014 January 8th, using the LGSAO system. A total exposure time of 4860 s was obtained with 27 exposures of 180 s each. Data were reduced and coadded with pipelines developed by Auger et al. (2008).

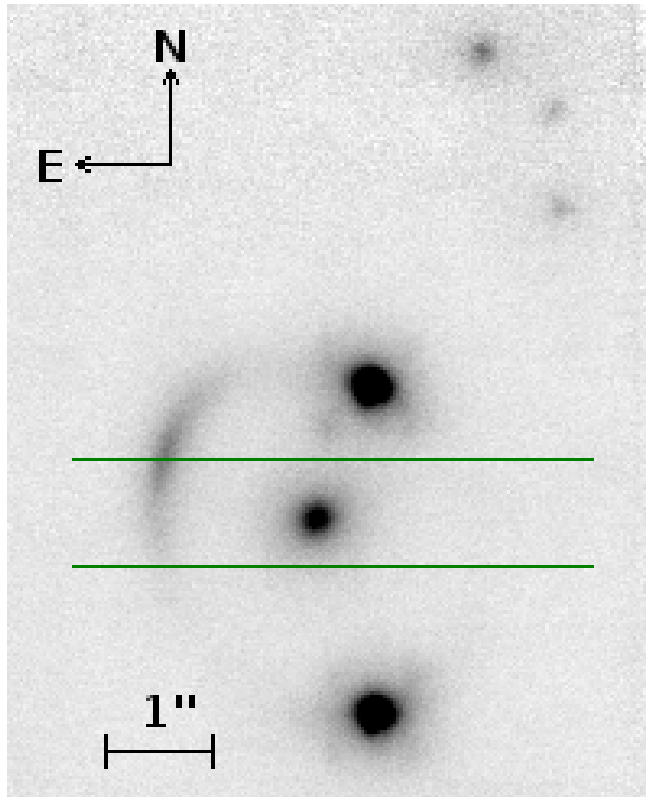

Figure 1. Imaging of SDSS J1206+4332 with LGSAO-NIRC2; North is up and East is left, the bar marks 1″. The two quasar images, the deflector galaxy ('G1' in Oguri et al. 2005; Eulaers et al. 2013) and the lensed host galaxy are all clearly visible. The lensed host traces a typical *fold* configuration, previously dubbed 'G3' and mistaken in the past for an additional galaxy along the line of sight. Three faint objects are visible to the NW, at ≈ 4.4″ from the deflector, dubbed 'G2' in previous observations where they were blended into a single, broad and faint object. The green horizontal lines mark the extent of the DEIMOS slit used for spectroscopy.

High resolution is obtained using the pixel scale of 9.94×10^{-3} arcseconds of the Narrow Camera of NIRC2.

The coadded data are shown in Figure 1, rebinned in three-by-three pixels to highlight low surface-brightness features. Here and through the rest of this paper, North is up and East is left. With this resolution, the two quasar images are clearly visible and distinguished from the deflector galaxy in the middle. The (lensed) host galaxy is visible around the quasar images and also in the *fold* arc at NE, which was previously mistaken for a distinct blue galaxy (dubbed 'G3'; Oguri et al. 2005; Eulaers et al. 2013).

We fit the deflector light with a flattened Sérsic profile, within a circular patch avoiding contamination from the Einstein ring light. To this aim, the model profile must be convolved with the point-spread function (PSF). Given the small field of view, there is no independent point source at our disposal for this purpose, so we must infer the PSF directly from the system itself. This is described in the subsection 2.1. The resulting parameters of the deflector light are given in Table 1. We will use the best-fitting light-profile in the following Sections to model the lensing and dynamics.

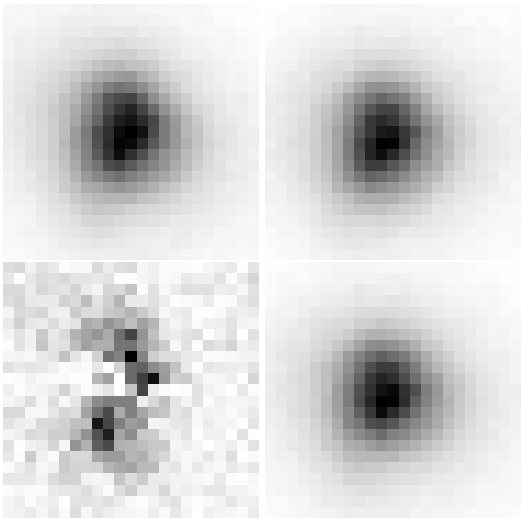

Figure 2. Cutouts around the two point-sources (top line), their scaled difference (bottom left) and first guess fo the PSF (bottom right) as decribed in Section 2.1.

b/a	p.a. (N of W)	n	$R_{\rm eff}$	Δra	Δdec
0.89	51.24 deg	2.66	$0.60''$	$0.252''$	$2.583''$

Table 1. Parameters of the best-fitting deflector light profile. From left to right: axis ratio, position angle (counterclockwise, N of W); Sérsic index; effective radius; relative astrometry from the southern-most quasar image, peak to peak, with r.a. (resp. dec.) increasing to the East (resp. North).

2.1 PSF estimation

For the deflector light subtraction, a first guess of the PSF is sufficient. We obtain it by isolating small cutouts centred on the two quasar images, subtracting to each of them the average flux around the border, normalizing their fluxes to unity, then coadding the two cutouts.

To recover a PSF that is common to both images and avoid propagating noise, we use a crude version of regularization. For each pixel of the target PSF coadd we consider the two corresponding pixel-values p_1, p_2 in the point-source cutouts: when these are within 0.1 of the average $av_p = (p_1 + p_2)/2$, we register av_p in the PSF coadd, otherwise we register the minimum $\min(p_1, p_2)$. The result is shown in Figure 2.

The reconstruction relies on the fact that the lensed host is stretched tangentially by gravitational lensing, so that in first approximation it contributes a uniform background flux to the point-source, which should dominate over the PSF light at large enough distances from the PSF core. A variant of this procedure will be combined iteratively with the lens model in Section 4.

3 KECK SPECTROSCOPY

Long-slit spectroscopic measurements of SDSS J1206+4332 were taken with the instrument DEIMOS (Faber et al. 2003) on Keck 2, on May 16 2015. The 1"-wide slit was centred on the deflector galaxy and aligned with the long axis in the E-W direction (see Fig. 1).

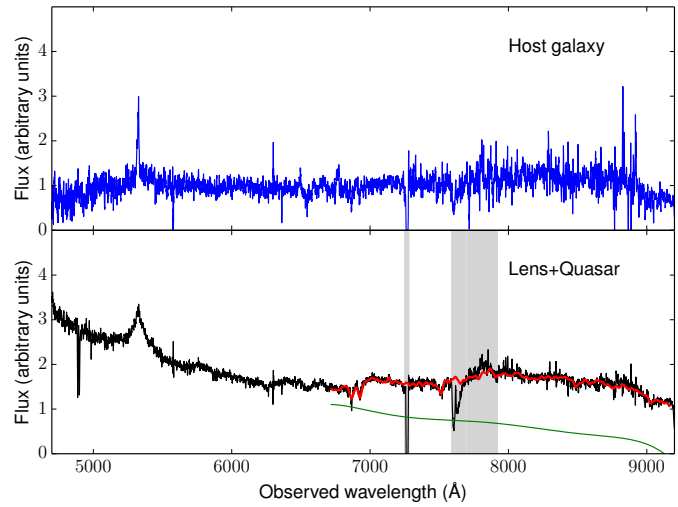

Figure 3. DEIMOS slit spectra. *Top:* Extracted 1D spectrum of the quasar host galaxy. *Bottom:* Extracted 1D spectrum of the quasar (northern point source) and the deflector galaxy. The red line is the best-fit spectrum obtained from the velocity dispersion fitting. The green line is the best-fit polynomial used to model continuum emission from the quasar. The vertical gray bands are regions of the spectrum masked out from the fit.

We used the 600ZD grism, covering the wavelength range 4600Å - 9200Å , with a spectral resolution of about 160 km s^{-1} FWHM. The total integration time was 1 hour. We detect a signal from the deflector galaxy, the quasar, and the quasar host. The lens galaxy and quasar host are spatially resolved, while the quasar itself, not covered by the slit, shows up as a contamination to the lens galaxy spectrum. The 1D spectra of the lens galaxy and quasar host are plotted in Figure 3.

The quasar component is visible with its continuum emission in the blue side of the lens galaxy spectrum and with broad emission lines. The host galaxy spectrum is very faint. The only clear line detected is [C III] 1908Å, also seen in the quasar component. However, while the quasar line is broad (FWHM $\sim$ 6000 km s^{-1}), the same line is much narrower in the spectrum of the host. Thus, we infer that the quadruply imaged part of the host galaxy does not include the compact broad line region, but only the significantly more extended narrow line region (NLR). In other words, the lens is acting as a natural "coronagraph", blocking out the light of the accretion disk and the BLR in two of the images. From a fit to the narrow line wavelength, we obtain a source redshift $z_s = 1.789$, confirming the one measured by Oguri et al. (2005). At lower signal-to-noise ratio, there is an absorption feature compatible with FeII at 2344Å at the host redshift z_s, which is seen also in the quasar spectrum.

The lens galaxy spectrum has some prominent stellar absorption features: Ca K,H at 3934Å, 3967Å, the G-band absorption complex around 4300Å, and Mgb at 5175Å, at a redshift $z_d = 0.745$. In addition to these stellar absorption lines we detect nebular absorption in the Mg II doublet 2795Å - 2803Å at $z = 0.748$. These lines were also detected by Oguri et al. (2005), who used them to estimate the lens redshift. There is a rest-frame velocity difference of about 516 km s^{-1} between stellar and Mg II absorption. We note

that this difference in redshift would introduce a small systematic bias in cosmological measurements (e.g. 0.15% in angular diameter distance to the deflector) based on this system if not corrected.

From the data at hand we can also extract a velocity dispersion measurement. We do this by fitting stellar templates to the observed spectrum, using an adaptation of the velocity dispersion fitting code by van der Marel et al. (1994) described by Suyu et al. (2010). We also fit for continuum emission from the quasar with a 7-order polynomial. We use G and F star templates from the Indo-US library. The 1D spectrum of the lens is extracted from a 1"×1.9" rectangular aperture. We fit the rest-frame wavelength region between 3800Å and 5250Å, where the most important stellar aborption features are found, masking out the region contaminated by broad MgII emission from the quasar as well as the deep atmospheric feature around 7600Å. The deepest stellar absorption lines, Ca K,H, fall in correspondance with the telluric absorption feature at 6900Å. We correct for this atmospheric absorption using a telluric standard star observation as a reference and keep Ca K,H in the region of the spectrum used for the fit. The best-fit spectrum is overploted in Figure 3. The median signal-to-noise ratio in the region used for the fit is 21Å^{-1}, though if we consider only the signal coming from the lens galaxy, i.e. once contamination from the quasar continuum emission is removed, it decreases to 13Å^{-1} (rest-frame).

We measure a velocity dispersion of $\sigma = 290 \pm 30$ km s^{-1}. The uncertainty reflects both statistical and systematic errors. We estimated the latter by repeating the fit over different wavelength ranges and by changing the order of the polynomial continuum.

4 LENS MODEL

We use the modelling code GLEE (Suyu & Halkola 2010; Suyu et al. 2012) to infer the lensing potential and reconstruct the extended source structure. As constraints, we use the arc surface-brightness distribution and the point source positions. The arc is cleaned from possible contamination by the lens light, by subtracting the best-fitting profile found in Section 2. Due to uncertainties in the PSF reconstruction, we artificially increase the pixel uncertainties around the point-source images, so that the lens model is constrained mainly by the NE fold and by the two quasar image positions, to which we assign a positional uncertainty of 20 mas. For computational simplicity, we consider just the pixels in an annular mask around the Einstein radius.

Inference on the lens mass profile relies primarily on the differential distortion and radial magnification of the same source patch on different sides of the lens. Then, two conditions must be met: (i) high resolution imaging, with good seeing conditions and small pixel size; (ii) a robust characterization of the PSF. While the former is satisfied by our Keck images, the latter is not directly available and the PSF must be reconstructed from the images.

The full model would then encompass both the lens parameters and the PSF reconstruction. We proceed iteratively, alternating PSF reconstruction and lens model fitting. From a run of the lens model, we get the predicted surface-brightness profile of the lensed host, which we can subtract near the quasar images. Similarly to the procedure in Section 2.1, we select two cutouts around the (host-subtracted) point-source images and combine their common pixel-values into a new PSF, which is then used in a new run of the lens model. Figure 4 shows the inferred PSF in subsequent iterations. After three iterations, the correction step starts to overfit noise, while the parameters of the lens model are not changing appreciably.

4.1 Model Components

We adopt a power-law profile for the total (i.e. luminous plus dark matter) mass density of the main deflector, with convergence

$$\kappa(x,y) = \frac{3-\gamma'}{1+q}\left(\frac{\sqrt{x^2+q^{-2}y^2}}{R_{\rm E}}\right)^{1-\gamma'} \quad (1)$$

along the principal axes of the deflector. With this convention, the Einstein radius $R_{\rm E}$ is such that in the circular limit ($q = 1$) it encloses a mean convergence of 1. In what follows, the model Einstein radii will be in angular units and denoted by θ_E.

The main deflector has a three nearby, faint perturbers to the NW, at a distance of approximately 4.4", as shown in Figure 1. In previous observations (Oguri et al. 2005; Eulaers et al. 2013), they were all blended into a single, broad and faint clump dubbed 'G2'. In order to model contributions from the immediate environment, we then include a Spherical Isothermal Sphere (SIS, $\gamma' = 2$, $q = 1$) centred on G2, with a centre to be adjusted, plus external shear. The role of shear is to correct for: flattening and/or imperfect centering of the group G2; lesser contributions from other galaxies in the vicinity of the lens; mismatch between the adopted and real flattening of the main deflector.

The model then has the following parameters: the power-law exponent γ' of the density profile of the deflector, its axis ratio q and position angle φ_l (N of W); the shear amplitude γ_s and position angle φ_s (N of W); the nearest perturber (G2) Einstein radius $\theta_{E,p}$ and its position; the source-position, constrained by the quasar image positions within a 20 mas range, and the point-source fluxes f_1, f_2. The point-source fluxes are computed but not used for the lens model, as they can be affected by source variability, microlensing, and milli-lensing by possible satellites of the main deflector. One final parameter would the Einstein radius $\theta_{E,l}$ of the main deflector, which we keep fixed because it can be determined with 1% precision as shown below.

4.2 Initialization and Choice of Parameters

Initialization is performed via conjugate-point analysis, i.e. identifying sets of points that should map to the same location in the source-plane and fitting for their predicted positions in the image-plane. Given the low number of constraints, we can examine just combinations of separate models, whose parameters will be cross-checked for consistency. The first initialized model has an isolated Singular Isothermal Ellipsoid (SIE, $\gamma' = 2$, $q < 1$), with free Einstein radius, axis ratio and position angle. The second model has a SIS plus external shear, the third has a SIS for the main deflector

model	$\theta_{\rm E,l}$ (arcsec)	q	φ_l [rad]	γ_s	φ_s [rad]	$\theta_{\rm E,p}$ (arcsec)	Δra (arcsec E)	Δdec (arcsec N)
SIE	1.61	0.807	0.65	—	—	—	—	—
SIS+XS	1.582	—	—	0.05	1.95	—	—	—
SIE+XS	1.582*	0.814	0.87	0.04	1.60	—	—	—
SIS+SIS	1.571	—	—	—	—	0.30	-2.506	3.485
SIE+SIS	1.571*	0.847	0.485	—	—	0.25	-2.198	3.852
all	1.575*	0.8*	0.75	0.034	1.12	0.25	-2.352*	3.669*
all	1.575*	0.86*	0.82	0.025	1.56	0.18	-2.352*	3.669*
all	1.575*	0.9*	0.91	0.032	1.89	0.17	-2.352*	3.669*
all	1.575*	0.99*	1.10	0.05	2.2	0.16	-2.352*	3.669*

Table 2. Model parameters obtained from conjugate-point analysis, using different models. Parameters marked by an asterisk are kept fixed during the optimization. These are then used to initialize a model with main lens, external perturber G2 and external shear, which is required to fit the quasar image positions and arc surface-brightness profile. The Einstein radius of the main lens is kept fixed to its SIS value when generalizing to SIE. The second part of the table shows results for a model with SIE, external shear and perturber, with some paramters fixed.

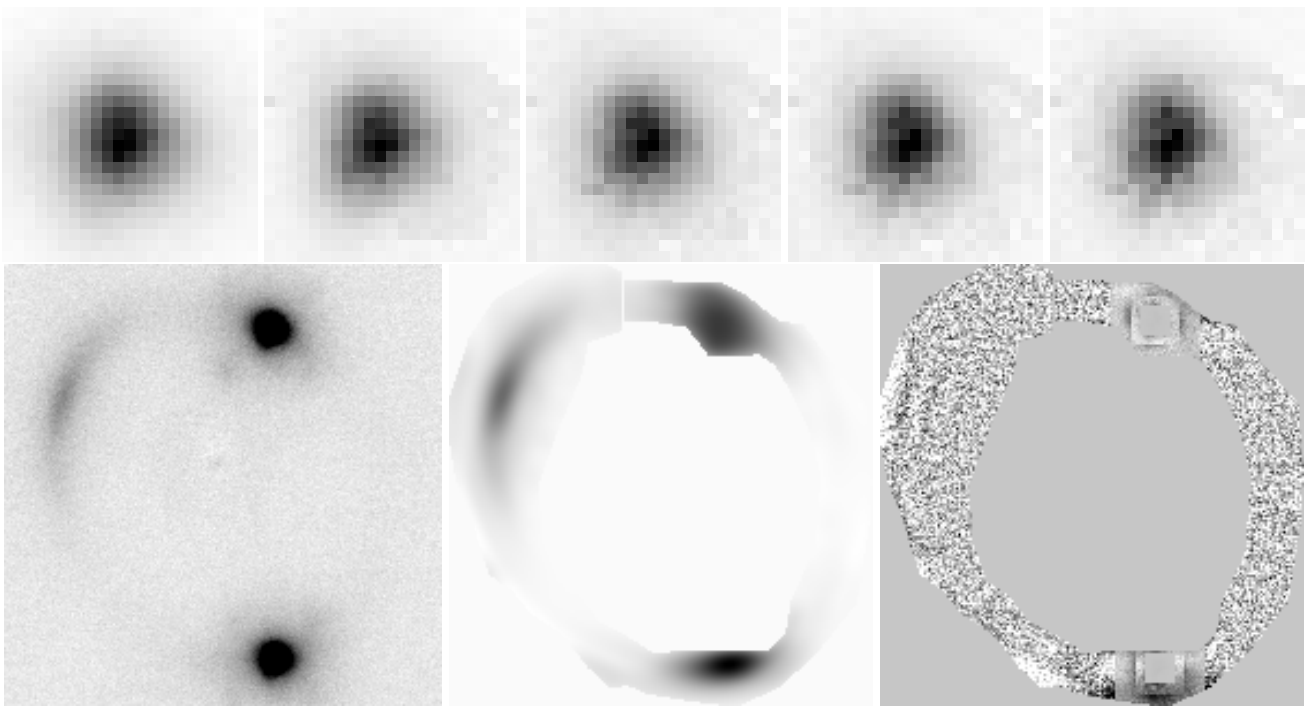

Figure 4. Reconstructed lens model. *Top:* iterative corrections of the reconstructed PSF. A 23-by-23 pixel cutout was chosen for the PSF; since the third iteration, the small-scale PSF corrections start to overfit noise in the data. *Bottom:* deflector-light-subtracted data (left), model of the arc (middle) and residuals over noise (right). Secondary lobes in the PSF are evident in the deflector-light-subtracted image and are masked out when fitting the extended structure. Secondary 'wings' in the reconstructed profile around the quasar images (near the mask border) are given by residuals in masking the PSF lobes out and choice of error-map. Their appearance is also degenerate with the point-source fluxes, which can create 'holes' in the reconstructed arc. The residuals on the fold arc are completely compatible with noise.

and one for G2. Since the SIS models yield consistent measurements of Einstein radius, we then generalize the main deflector to a SIE, keeping its $R_{\rm E}$ to the SIS value, and optimize a model with external shear and one with a SIS for the external perturber G2.

The results are shown in Table 2. The position of G2 is consistent within $\approx 0.4''$. Its inferred inferred values of θ_E are consistent within 0.05". The difference in $\theta_{\rm E,l}$ between a model with external shear and a model with external SIS perturber is $\approx 0.01''$.

The interplay between different parameters is explored by different choices of flattening of the main deflector, keeping the perturber position fixed to the average value between the SIS+SIS and SIE+SIS cases. Results from this experiment are shown in the second half of Table 2. When $q = 0.9$ as derived from the photometry of the deflector galaxy in Sect. 2, the inferred deflector p.a. from lensing is exactly the same as the one found from the photometry. This finding suggests that $q = 0.9$ and $\varphi_l = 0.91$ can be kept fixed in the lens model. Similarly, we keep the perturber position

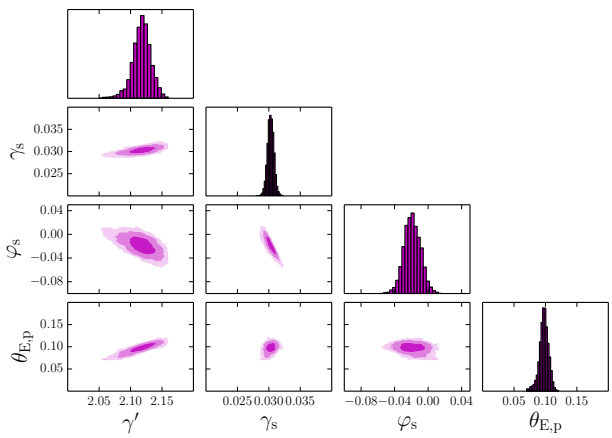

Figure 5. Reconstructed lens model. Inference on the four main parameters of the lens model. We show the marginalized posterior distribution of the power-law slope γ', external shear amplitude γ_s and angle φ_s, and the perturber (G2) Einstein radius $\theta_{\rm E,p}$ in arcseconds. Due to the very small pixel-size and lack of independent PSF, the model uncertainties are artificially small.

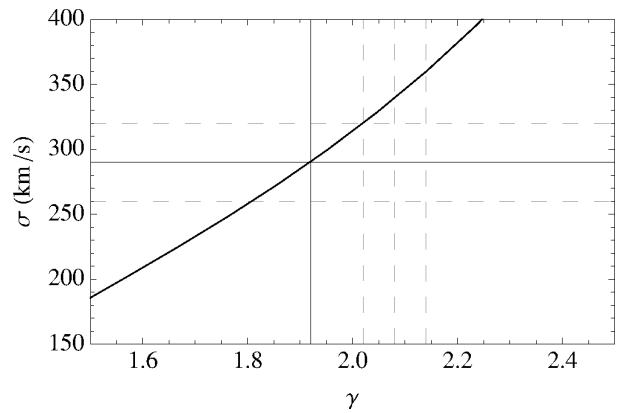

Figure 6. Combined inference from lensing and dynamics. The model velocity dispersion is plotted against total density exponent $\gamma' = -\mathrm{d}\log\rho/\mathrm{d}\log r$, corresponding to the measured Einstein radius $\theta_{\rm E,l} = 1.575''$. We also show the measured velocity dispersion with its uncertainty (horizontal lines) and the density exponent from the lens model, with a conservative uncertainty of 5% (vertical lines).

fixed, since possible corrections will be given by the shear term.

Unfortunately, with the data at our disposal, a complete lens model on the extended source is unstable and some of the parameters converge to pathological minima. For this reason, we are currently forced to keep some of the parameters fixed to their fiducial values.

4.3 Lensing Results

Results from the model are shown in Figure 5, showing the inferred posterior distribution on the four main parameters. Their values are in general agreement with what is found at the initialization stage. The Einstein radius $\theta_{\rm E,p}$ of G2 is small but non negligible. Other perturbations to the lensing potential are summed up in a small shear, which corroborates our working hypothesis. The density slope $\gamma' = 2.04$ is in line with the general description of early-type galaxy lenses (Koopmans et al. 2009), but steeper than the median value ≈ 1.95 of lens galaxies at this redshift (Sonnenfeld et al. 2013).

The statistical uncertainties are driven by the small pixel size compared to the Einstein radius, and are therefore dominated by systematics in the choice of lens model, PSF correction scheme, and estimation of errors near the point-source images. Results on other systems with HST data, with a robustly characterized PSF and deeper observations on the Einstein ring, typically yield uncertainties around $2-3\%$ on γ' (Dye & Warren 2005; Suyu et al. 2013). In what follows, we will adopt an estimated 5% for the uncertainties on γ'.

Galaxies in the vicinity of the main deflector contribute to the deflections of light-rays. As a first approximation, their role can be subsumed in a uniform sheet of convergence κ_e around the main deflector. However, this can be reabsorbed by (unobservable) shifts and rescalings in the source-plane, so that κ_e cannot be determined from lensing alone. This *mass-sheet degeneracy* (MSD, Falco et al. 1985) is a simple case of source-position transformation degeneracies (Schneider & Sluse 2013), with particular importance for time-delay cosmography. Bounds on κ_e can be put by studying the environment of the lens (Fassnacht et al. 2011; Greene et al. 2013). Oguri et al. (2005) have shown that the environment of SDSS J1206+4332 is comparable to a random field of view, considering galaxies within 1 arcmin from the lens down to an $I-$band magnitude of 24. Then, given the current data quality, we can neglect κ_e for our purposes. We will discuss this choice further in the following Sections.

5 DYNAMICS

Information on the kinematics of stars in the deflector yields and independent mass probe, thus breaking residual degeneracies in the lens model (Treu & Koopmans 2002, 2004). This is especially true for the power-law profiles used here, for which simple relations hold between the velocity dispersion and power-law exponent (Koopmans 2006). From gravitational lensing, a normalization condition holds for the projected mass of the lens within the Einstein radius:

$$M_p(R_E) = (1-\kappa_e)\pi R_E^2 \Sigma_{cr} \;=\; \frac{c^2 D_s}{4GD_l D_{ls}}(1-\kappa_e)R_E^2 \;. \quad (2)$$

In terms of the mass $M(r)$, surface-brightness $\Sigma(R) = \Sigma_0\tilde{\Sigma}(R/R_{\rm e})$ and 3D luminosity $\nu(r) = \tilde{\nu}(r/R_{\rm e})\Sigma_0/R_{\rm e}$ profiles, the line-of-sight velocity dispersion $\sigma_p(R)$ satisfies

$$\Sigma(R)\sigma_p^2(R) \;=\; 2G\int_R^\infty \frac{\nu(r)M(r)}{r^2}(\sqrt{r^2-R^2}+k_\beta(r,R))\mathrm{d}r \quad (3)$$

where the kernel k_β depends on the orbital anisotropy profile $\beta(r)$ (Mamon & Łokas 2005; Agnello et al. 2014). In the power-law case, with $\rho(r) \propto r^{-\gamma'}$, the lensing mass normal-

ization yields

$$\tilde{\Sigma}(R/R_{\rm e})\sigma_p^2(R) \;=\; (1-\kappa_e)c^2\frac{D_sR_E}{D_{ls}D_l}\times\frac{(3-\gamma')\Gamma(\gamma'/2)}{\sqrt{\pi}\Gamma((\gamma'-1)/2)}\times \quad (4)$$
$$\frac{R_{\rm e}^{2-\gamma'}}{R_E^{2-\gamma'}}\int_{R/R_{\rm e}}^{\infty}\tilde{\nu}(x)x^{-\gamma'}\left(\sqrt{x^2-(R/R_{\rm e})^2}+\tilde{k}_\beta(x,R/R_{\rm e})\right){\rm d}x$$

The model velocity dispersion can be averaged over the slit or aperture to be directly compared with its measured value, either via numerical integration or with the more compact formalism of Agnello et al. (2013), which is adequate here because most of the deflector light is enclosed in the DEIMOS slit. Then, given $\theta_E = R_E/D_l$ and the distance-ratio D_s/D_{ls}, from the measured kinematics one can derive the exponent γ' and *vice versa*. In Figure 6 we show the predicted velocity dispersion as a function of γ', together with the measured value and the density exponent inferred from the lens model.

Figure 6 shows the predicted velocity dispersion σ as a function of γ'. The vertical lines delimit the 68% confidence interval in γ' predicted by the lens model, while the horizontal lines show the measured σ with its 68% confidence interval. The data are not sufficient to discriminate between models with different anisotropy, since we just have an aperture-averaged value (with broad PSF) instead of a radial profile at our disposal.

The slope obtained this way, $\gamma' = 1.93 \pm 0.09$, is smaller than the value inferred from lensing alone. Still, when a conservative uncertainty of 5% on the lensing γ' is adopted, the two results are compatible within 68% confidence level.

6 PROSPECTS FOR COSMOGRAPHY

The time-variability of the source quasar provides an additional observable, which is the time-delay between the two quasar images. The arrival time is given by

$$t \;=\; (1+z_d)\frac{D_sD_d}{cD_{ds}}\left[(\mathbf{x}_I-\mathbf{x}_S)^2-\psi(\mathbf{x}_I)\right] \quad (5)$$

in terms of the projected lens potential ψ, deflection $\mathbf{x}_I - \mathbf{x}_S$ and cosmological distances.

From the lens model, the predicted time-delay can be compared with its measured value to infer the time-delay distance $D_{\Delta t} = (1+z_d)D_lD_s/D_{ds} \propto H_0^{-1}$, or equivalently the cosmological parameters, primarily the Hubble constant. This is generally plagued by the MSD, as the source-position transformation that eliminates κ_e from the lens model produces a biased measurement $H_0/(1-\kappa_e)$ of the Hubble constant, with everything else fixed – cosmological abundances and measured Δt. If the velocity dispersion and time-delay are modelled jointly, the common dependence on $(1-\kappa_e)D_s/D_{ds}$ cancels out, so that the angular-diameter distance D_d to the deflector is inferred directly, with possible systematics from κ_e now erased (Jee et al. 2014). Alternatively, in presence of a good prior on κ_e, dynamics can be used to obtain the exponent γ' to be used in the time-delay inference, since the model kinematics depend just weakly on cosmological parameters (eq. 4).

Given the data presented here, with small nominal uncertainties on γ', one would be tempted to exploit them for time-delay cosmography. We caution against that, for the following reasons. First, the signal-to-noise ratio of faint features, such as the fold arc and perturbers in G2, is too low to enable a flexible model with robustly determined parameters. Second, the lack of an independent PSF model leaves degeneracies in the lens model unresolved, degrading the predictive power near the point-source positions. This is particularly true for two-quasar-image systems like SDSS J1206+4332; in four-quasar-image systems, there is more information from the four quasars to reconstruct the PSF directly from the lens system (Chen et al., in preparation). The confidence ranges of lensing parameters account just for the statistical uncertainties and are driven mainly by the small pixel-size, whereas systematic uncertainties (e.g. from PSF correction) dominate the error budget.

Bearing the caveats in mind, it is interesting to provide some rough cosmographic estimates and discuss what can be earned from more reliable data. For concreteness, we forecast the cosmographic constraints that we expect to obtain with (1) HST imaging that have better characterized PSFs, and (2) spatially resolved kinematics of the deflector galaxy that help break lens-modeling and mass-sheet degeneracies. To estimate the precision on the time-delay distance, we assume uncertainties on the time delays of 3% (Eulaers et al. 2013), modeling with HST imaging of 3% (e.g., Suyu et al. 2013), and external convergence κ_e of 4% (e.g., Greene et al. 2013, Collett et al. 2013). Adding these contributions in quadrature, we forecast an uncertainty of 5.8% on $D_{\Delta t}$. For reference, we adopt a fiducial value for $D_{\Delta t}$ which corresponds to a fiducial flat ΛCDM model with $\Omega_{\rm m} = 1-\Omega_\Lambda = 0.3$ and $H_0 = 70\,{\rm km\,s^{-1}Mpc^{-1}}$. Assuming a Gaussian probability distribution for $D_{\Delta t} = 5789 \pm 336$ Mpc, we show in Figure 7 the cosmographic information from SDSS J1206+4332 assuming Planck priors (Planck Collaboration et al. 2014) in either open ΛCDM cosmology (left panel) and flat wCDM cosmology (right panel). Such a distance measurement of $D_{\Delta t}$ for SDSS J1206+4332 would help break significantly parameter degeneracies in the CMB data, and provide an independent test of systematics in cosmographic probes.

7 SUMMARY

We have presented laser guide star adaptive optics images and spectroscopic observations of the gravitational lens system SDSS J1206+4332. A precise time delay measurement is available for this doubly imaged quasar (Eulaers et al. 2013), making it a prime target for follow-up observations aimed at using it as tool for cosmography. The high resolution images allow us to recognize that the system is in a very unusual and favorable configuration for cosmography, previously not resolved in seeing based images. Furthermore, our deep Keck spectroscopy allows to correct the previous estimate of the redshift of the main deflector and measure its stellar velocity dispersion based on stellar absorption features. We then use the newly available information to construct a gravitational lens model of the system and discuss its potential for cosmography. Our main results can be summarized as follows:

- The quasar lies just outside of the astroid caustic in the source plane and is thus doubly imaged. However, the quasar host galaxy crosses the caustic and produces two additional merging images in a classic fold configuration – previously mis-identified as an unrelated galaxy along the line

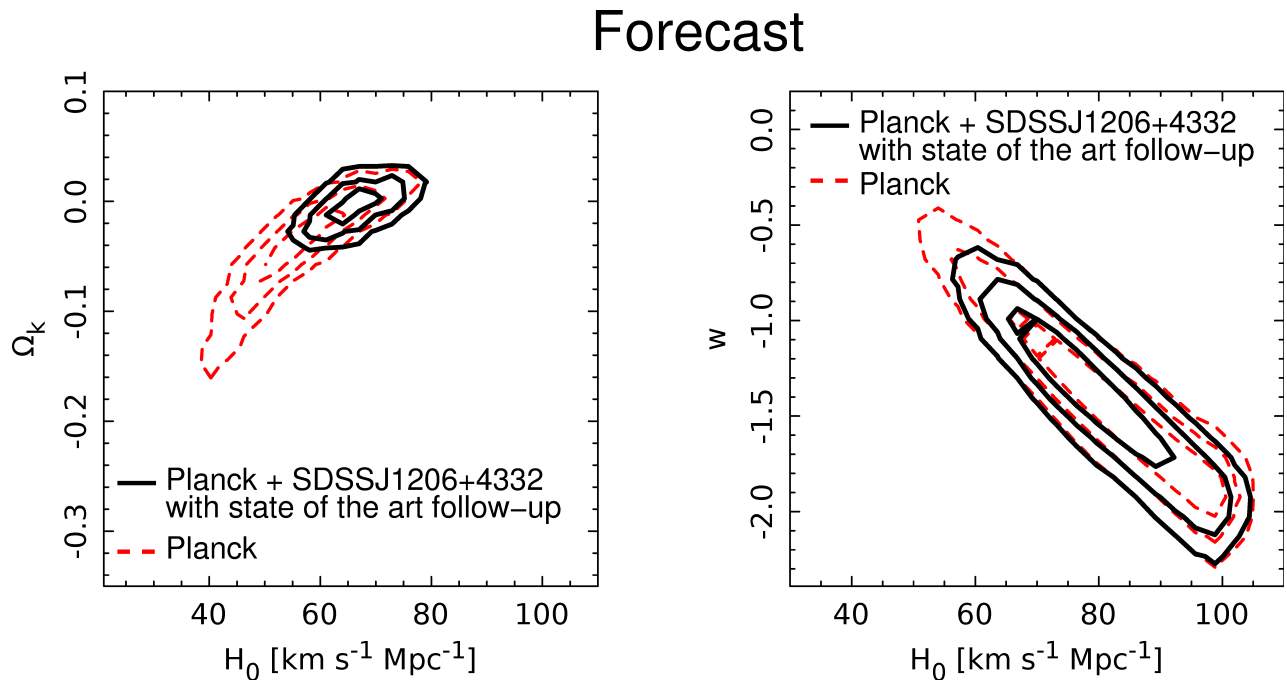

Figure 7. Predicted inference on cosmological parameters, in presence of robust model parameters (with well controlled systematics) from more reliable data than the ones available here. Dashed red lines are the Planck prior on cosmological parameters (Planck Collaboration et al. 2014), the black lines are the marginalized posterior using SDSS J1206+4332 as a cosmographic probe, *assuming state of the art follow-up data are available*. Degeneracies between H_0 and other cosmological parameters are appreciably reduced by time-delay lenses, which probe primarily H_0. *Left:* Open ΛCDM cosmology (free curvature parameter Ω_k). *Right:* Flat CDM ($\Omega_k = 0$) with free equation of state parameter w.

of sight in seeing limited images. The presence of two additional images doubles the amount of information available to constrain the gravitational lens model.

• The lensing geometry acts as a natural "coronagraph", blocking out the light coming from the broad line region and the accretion disk in two of the images. Thus, those two images give a very clear view of the narrow line region surrounding a $z = 1.79$ quasar. This system represents an interesting target for follow-up studies with an integral field spectrograph.

• A small group of galaxies is identified near the main deflector and included in the mass model. The group of galaxies had previously been misidentified as a single galaxy in seeing limited images.

• The redshift of the main deflector is measured to be $z = 0.745$ from stellar absorption features, revising the previous estimate pf $z = 0.748$ based on an intervening Mg II absorber.

• The stellar velocity dispersion of the main deflector is measured to be 290 ± 30 kms^{-1}.

• Modeling the surface brightness distribution of the lensed source requires an accurate model of the PSF. As no stellar image is available in the narrow field of view of NIRC2 we use an iterative procedure to reconstruct the PSF from the lensed quasar images themselves.

• We construct lens models of the system, including nearby perturbers in addition to the main deflector. The models reproduce the data for a close-to-isothermal total mass density profile of the main deflector. Some of the lens model parameters suffer from relatively large uncertainties dominated by residual PSF uncertainties.

• We combine the lensing and dynamical information to estimate the logarithmic slope of the total mass density profile γ'. We find $\gamma' = 1.93 \pm 0.09$ consistent with typical values found for massive early-type galaxies at these redshifts.

• We estimate that the current systematic uncertainties of the mass model of this system are too large to provide any interesting cosmographic inference. However, we show that, with the addition of HST images and spatially resolved stellar velocity dispersion, the system would become very useful. As an illustration we combine the simulated lensing likelihood with the Planck prior, and show that the uncertainty on w, curvature and H_0 is significantly reduced.

ACKNOWLEDGMENTS

AA, AS, TT, and CDF acknowledge support from NSF grants AST-1312329 and AST-1450141 "Collaborative Research: Accurate cosmology with strong gravitational lens time delays". AA, AS, and TT gratefully acknowledge support by the Packard Foundation through a Packard Research Fellowship to TT. S.H.S. acknowledges support from the Ministry of Science and Technology in Taiwan via grant MOST-103-2112-M-001-003-MY3.

Data presented in this paper were obtained at the W.M. Keck Observatory, which is operated as a scientific partnership among the California Institute of Technology, the University of California, and the National Aeronautics and Space Administration. The Observatory was made possible by the generous financial support of the W. M. Keck Foundation. The authors also recognize and acknowledge the very

significant cultural role and reverence that the summit of Mauna Kea has always had within the indigenous Hawaiian community. We are most fortunate to have the opportunity to conduct observations from this mountain.

REFERENCES

Agnello, A., Auger, M. W., & Evans, N. W. 2013, MNRAS, 429, L35
Agnello, A., Evans, N. W., & Romanowsky, A. J. 2014, MNRAS, 442, 3284
Auger, M. W., Fassnacht, C. D., Wong, K. C., et al. 2008, ApJ, 673, 778
Burud, I., Hjorth, J., Courbin, F., et al. 2002, AA, 391, 481
Chantry, V., Sluse, D., & Magain, P. 2010, AA, 522, A95
Collett, T. E., Marshall, P. J., Auger, M. W., et al. 2013, MNRAS, 432, 679
Dye, S., & Warren, S. J. 2005, ApJ, 623, 31
Eulaers, E., Tewes, M., Magain, P., et al. 2013, AA, 553, A121
Faber, S. M., Phillips, A. C., Kibrick, R. I., et al. 2003, Proc. SPIE, 4841, 1657
Falco, E. E., Gorenstein, M. V., & Shapiro, I. I. 1985, ApJL, 289, L1
Fassnacht, C. D., Koopmans, L. V. E., & Wong, K. C. 2011, MNRAS, 410, 2167
Fassnacht, C. D., Xanthopoulos, E., Koopmans, L. V. E., & Rusin, D. 2002, ApJ, 581, 823
Greene, Z. S., Suyu, S. H., Treu, T., et al. 2013, ApJ, 768, 39
Jackson, N. 2007, Living Reviews in Relativity, 10, 4
Jee, I., Komatsu, E., & Suyu, S. H. 2014, arXiv:1410.7770
Keeton, C. R., & Zabludoff, A. I. 2004, ApJ, 612, 660
Koopmans, L. V. E., Garrett, M. A., Blandford, R. D., et al. 2002, MNRAS, 334, 39
Koopmans, L. V. E., Treu, T., Fassnacht, C. D., Blandford, R. D., & Surpi, G. 2003, ApJ, 599, 70
Koopmans, L. V. E. 2006, EAS Publications Series, 20, 161
Koopmans, L. V. E., Bolton, A., Treu, T., et al. 2009, ApJL, 703, L51
Mamon, G. A., & Łokas, E. L. 2005, MNRAS, 363, 705
McCully, C., Keeton, C. R., Wong, K. C., & Zabludoff, A. I. 2014, MNRAS, 443, 3631
Oguri, M., Inada, N., Hennawi, J. F., et al. 2005, ApJ, 622, 106
Oguri, M. 2007, ApJ, 660, 1
Paraficz, D., & Hjorth, J. 2009, AA, 507, L49
Pérez-Ràfols, I., Miralda-Escudé, J., Lundgren, B., et al. 2015, MNRAS, 447, 2784
Planck Collaboration, Ade, P. A. R., Aghanim, N., et al. 2014, AA, 571, A16
Refsdal, S. 1964, MNRAS, 128, 307
Schechter, P. L., Bailyn, C. D., Barr, R., et al. 1997, ApJL, 475, L85
Schneider, P., & Sluse, D. 2013, AA, 559, A37
Sonnenfeld, A., Treu, T., Gavazzi, R., et al. 2013, ApJ, 777, 98
Suyu, S. H., Marshall, P. J., Auger, M. W., et al. 2010, ApJ, 711, 201
Suyu, S. H., & Halkola, A. 2010, AA, 524, A94
Suyu, S. H., Hensel, S. W., McKean, J. P., et al. 2012, ApJ, 750, 10
Suyu, S. H., Auger, M. W., Hilbert, S., et al. 2013, ApJ, 766, 70
Suyu, S. H., Treu, T., Hilbert, S., et al. 2014, ApJL, 788, L35
Tewes, M., Courbin, F., Meylan, G., et al. 2013, AA, 556, A22
Treu, T., & Koopmans, L. V. E. 2002, MNRAS, 337, L6
Treu, T., & Koopmans, L. V. E. 2004, ApJ, 611, 739
van der Marel, R. P., Rix, H. W., Carter, D., et al. 1994, MNRAS, 268, 521
Wizinowich, P. L., Le Mignant, D., Bouchez, A. H., et al. 2006, PASP, 118, 297
Wucknitz, O., Biggs, A. D., & Browne, I. W. A. 2004, MNRAS, 349, 14